Design of an optics system for the short-HIBEAM beamline at the European Spallation Source

Author
Marianne Kuhl

Supervisor
Valentina Santoro

Co-supervisors
Matthias Holl
Linus Persson

Lund University
Department of Physics
Division of Particle and Nuclear Physics

15 credits, 1 semester half-time equivalent
Thesis submitted for the degree of Bachelor of Science
June 2026

Abstract

Dark matter remains a largely elusive phenomenon, particularly its composition. Several candidate particles have been proposed, including axions and axion-like particles (ALPs). Detection of axions and ALPs have been attempted but none so far have yielded positive results. The High Intensity Baryon Extraction and Measurement instrument (HIBEAM) at the European Spallation Source (ESS) will be used to attempt ALP detection using Ramsey interferometry with increased sensitivity by 2-3 orders of magnitude compared to current performance of other experiments. In order to maximize the sensitivity of the search, HIBEAM's neutron guide must be optimized. The optimization of this guide is the subject of this thesis. The work was carried out using McStas, a neutron ray-tracing simulation framework that employs Monte Carlo sampling to model neutron transport through instrument components. The optimal guide specifications were determined to be a supermirror reflectivity of $m = 4$, together with a selective collimation of the high-intensity region of the beam placed 15 m from the source to match the 10 cm diameter constraint of the polarizer at the end of the neutron guide section. These specifications were determined based on the maximization of a simplified figure of merit NT^2, where N is the neutron intensity and T is the time of flight in the neutron guide. By maximizing this quantity, the uncertainty in the Ramsey fringes is minimized.

Acknowledgments

I would like to express my deepest appreciation to my thesis supervisor, Valentina Santoro, for providing me with the opportunity to complete my thesis with her research group, and for her continuous support throughout the duration of my thesis.

This endeavor would not have been possible without my co-supervisors, Matthias Holl and Linus Persson. They were extremely helpful and patient with all my questions.

Many thanks to the HIBEAM-NNBAR research group for the opportunity to complete my thesis with them and for the opportunity to attend the weekly meetings which enabled me to gain first-hand experience of what being part of a research group is like.

I would like to extend my sincere thanks to God, my family, and my friends. I could not have done it without your support.

Glossary

ALP Axion-Like Particle. 1, 4

CMS Cryogenic Moderator System. 4

DM Dark Matter. 4

HIBEAM High-Intensity Baryon Extraction and Measurement. 4, 5

ILL Institut Laue Langevin. 5

McStas Monte carlo Simulation of triple axis spectrometers, a programming package for neutron-ray tracing simulations. 11

PSD Position Sensitive Detector. 13

QCD axion Quantum Chromodynamics axion. 7

RF Radiofrequency. 4

ULA Ultra Light Axion. 7

Contents

1 Introduction

Cosmological phenomena, such as gravitational lensing, rotation curves of axisymmetric systems, the virial theorem and others [1], have led to the postulation of the existence of dark matter (DM), which is not explained by the Standard Model. Although the existence of DM is strongly substantiated by the aforementioned phenomena, very little is known about its composition. This has led to several candidate particles being proposed as being the constituents of DM. One such candidate is the axion-like particle (ALP). The axion was originally introduced to solve a particularly compelling problem: the strong CP problem [2]. The strong force conserves the CP symmetry despite not being required by the Standard Model. In addition, the axion is a well-motivated dark matter candidate, and its discovery would provide strong evidence for physics beyond the Standard Model.

The High Intensity Baryon Extraction and Measurement (HIBEAM) project at the European Spallation Source (ESS) aims, among other experiments, to detect ALPs using Ramsey interferometry [3]. Ramsey interferometry detects ALPs by measuring the phase shift accumulated by neutron spins between the initial and final applications of a radiofrequency (RF) pulse. This is determined by observing the polarization of the neutrons and determining if a relative phase change occurred. This experimental technique requires high precision and sensitivity. The sensitivity can be improved by ensuring that the neutrons spend as much time as possible precessing between the two applications of RF pulses, as well as maximizing the neutron intensity.

This experiment will be carried out using the short-HIBEAM beamline, an initial phase of the full HIBEAM programme that will become operational earlier. The short-HIBEAM beamline will be 25 m long, including a 10 m long magnetically shielded region where the Ramsey setup will be located. Prior to the Ramsey region, a neutron optics guide system transports neutrons from the ESS source to the experimental area. This thesis presents the design of this neutron optics to maximise sensitivity of the Ramsey interferometry technique for detecting ALPs.

This optimization process was carried out using a model of short-HIBEAM in the neutron-ray tracing software McStas [4]. Several variables and configurations were tested, including material reflectivity and beam collimation.

2 Theory

2.1 The European Spallation Source

ESS is a research facility in Lund, Sweden. It produces neutrons by spallation, which can then be subsequently used in various experiments as probes. The neutron production process proceeds as follows. Hydrogen gas is ionized to form a plasma of protons and electrons. The protons are extracted, accelerated, and directed in pulses onto a rotating tungsten target, where neutrons are produced via spallation[5]. Subsequently, the neutrons are moderated using the Cryogenic Moderator System (CMS) [6] and subsequently directed to the beamlines. The CMS is known as the Butterfly Moderator due to its butterfly-like shape as shown in Figure 1. The resulting neutrons are primarily thermal and cold neutrons [7]. The spallation target and the moderator are contained inside an area known as the monolith, which is a structure with a thickness of approximately 3.5 m around the target, that serves to shield from the ionising radiation produced by the spallation [8].

Surrounding the monolith is a structure known as the bunker, which is made of heavy magnetite concrete. Its walls are approximately 3.5 m thick, and its internal volume extends about 11.5 m from the target in the North and East sectors, and up to 24.5 m in the South and West sectors [9]. It serves to shield the instrument area from the ionizing radiation produced by the spallation process.

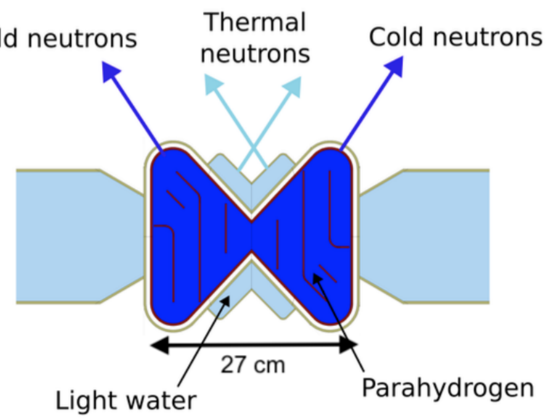

Figure 1: Top view of the ESS moderator, often referred to as the ESS butterfly. Credit: Figure adapted from geometry courtesy of ESS.

The neutrons are directed to various beam ports, which can be connected to a beamline, joining the target region and the instrumental region. This thesis focuses on the optimization of the guide section for the HIBEAM beamline, which will be located at beamport E5.

2.2 The High Intensity Baryon Extraction And Measurement beamline

The High Intensity Baryon Extraction And Measurement (HIBEAM) beamline is a proposed project at ESS dedicated to particle physics experimentation. In order to maximise the use of this instrument and begin operations sooner, an initial phase of the beamline, known as the short-HIBEAM has also been proposed. Once this phase is complete, it will be expanded to the full HIBEAM.

HIBEAM will primarily search for baryon number violation, as well as searching for ultralight axion-like particles, and for a neutron electric dipole moment [10]. HIBEAM is expected to achieve an order-of-magnitude improvement in sensitivity for baryon number violation searches compared to previous experiments performed at the Institue Laue-Langevin (ILL) [11]. This greater sensitivity will be partially provided by the improvement in the time-averaged neutron flux [7], but requires further improvements, including the neutron optics. In short, the ESS and specifically the HIBEAM project aims to deliver significant progress in some of the most important open questions of modern physics [10].

The short-HIBEAM set-up for the axion search would function as follows. Neutrons are extracted from the moderator. The neutrons pass through the neutron guide. A chopper is used to shape the neutron pulse by selecting neutrons within a specific velocity range [12]. Next, the beam is collimated before entering a 10 m long magnetically shielded region. A constant magnetic field B_0 is applied in this region. Before allowing the beam to enter this region, the polarizer ensures that the neutron spins are aligned with this B_0 field. The spins are then rotated $\frac{\pi}{2}$ by a RF coil operating at a field of strength B_1 at a frequency ω_1. The difference between ω_1 and the Larmor frequency $\omega_L = \gamma B_0$ is known as the detuning $\Delta = \omega_1 - \omega_L$. The neutrons are then allowed to precess in the 10 m region before the RF pulse is applied again. Finally, the analyzer detects the polarization of the neutrons. The prospective set-up is shown below in Figure 3.

This set-up and experiment is expected to provide an improvement of 2-3 orders of magnitude in the sensitivity compared to the current best laboratory limits [13].

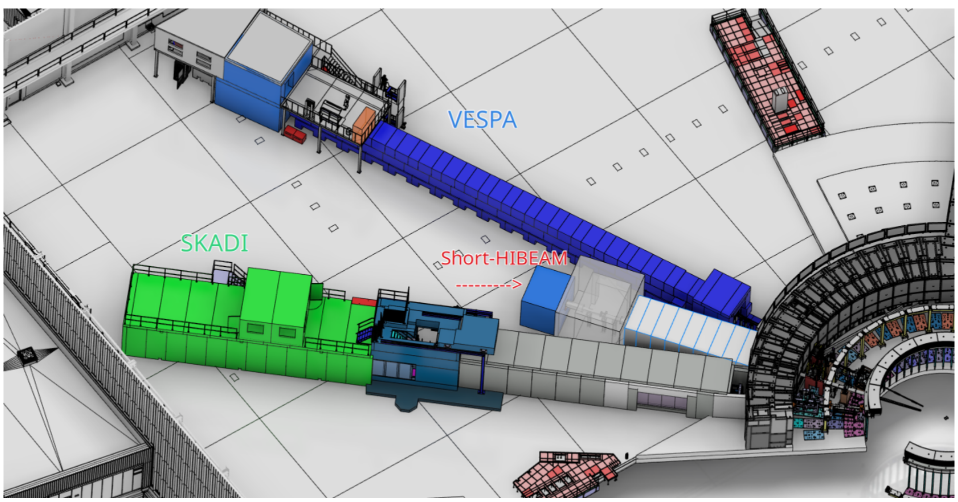

Figure 2: CAD rendering of the planned short-HIBEAM beamline. Credit: Madalin Alexandru Bartis and Linus Persson.

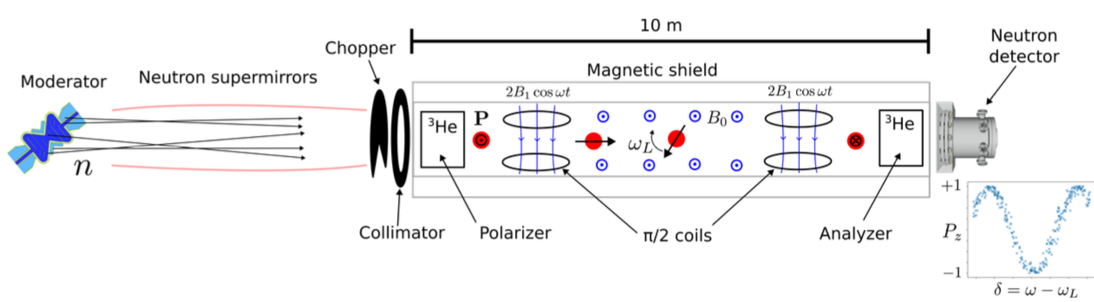

Figure 3: Conceptual sketch of prospective set-up for the detection of axions with the short-HIBEAM at ESS. Credit: Linus Persson.

2.3 Axions and Dark Matter

DM is estimated to account for around 25% of the critical density of the Universe, or 85% of the total matter density of the universe[1]. The interpretation of astrophysical and cosmological observations as evidence for dark matter assumes that gravity is correctly described by General Relativity on large scales. Although DM is not directly detectable, its existence is inferred from the effect it has on classical matter [1]. Although there is strong evidence for the existence of DM, its composition is not known and several candidates have been postulated.

Axions (also known as Quantum Chromodynamics (QCD axion) axions), Axion-Like Particles (ALP) and Ultralight Axions (ULA) are all possible candidates for dark matter constituents. Each of these particles is distinct but they are related to one another. ULAs are a subclass of ALPs. The QCD axion, originally introduced to solve the strong CP problem, has well-defined couplings, including interactions with gluons. More general ALPs share similar effective descriptions and may play a role in dark matter, but they do not necessarily couple to gluons and therefore do not address the strong CP problem [14].

The strong CP problem arises from the fact that the Standard Model allows for CP-violating terms in QCD, yet no such violation has been observed experimentally [15]. While the QCD axion is a compelling dark matter candidate, it can only account for the observed dark matter density within a limited range of masses. In contrast, ALPs span a much broader parameter space, including ultralight masses, and arise in many extensions of the Standard Model [16]. HIBEAM is primarily sensitive to ALPs rather than the QCD axion.

2.4 Ramsey Interferometry

Axions and ALPs can be searched for through several experimental approaches, including collider experiments such as the Large Hadron Collider (LHC) at CERN. However, collider experiments are primarily sensitive to heavier ALPs with relatively strong couplings, and are generally not well suited for searches for ultralight axions due to their extremely small masses and weak interactions [17]. Ramsey interferometry like in this proposed work instead relies on neutron spin precession to search for axions. This method was chosen because it provides high sensitivity over a broad range of axion masses compared to many other experimental approaches [18].

The coherently oscillating classical field of the axion can be described as:

$$a(t) = a_0 \cos(\omega t), \tag{1}$$

where

$$\omega = \frac{m_a c^2}{\hbar}, \tag{2}$$

where m_a is the axion mass, c is the speed of light in vacuum and $\hbar$ is the reduced Planck constant.

The interaction of an axion with a nucleon is described as:

$$\mathcal{L}_{\text{int}} = -\frac{C_N}{2f_a}\, \partial_\mu a\, \bar{N}\gamma^\mu\gamma^5 N, \tag{3}$$

where C_N is a dimensionless parameter, f_a is the axion decay constant, ∂_μ is the partial derivative with respect to μ where μ is a label taking on the values 0 to 3 referring to t,x,y or z respectively, a is the axion field, N is the nucleon field, $\bar{N}$ is its Dirac adjoint, and γ are the Dirac gamma matrices [13].

The Ramsey interferometry setup consists of two spatially separated regions where an oscillating radiofrequency field is applied, with a field-free region in between. In the first region, an RF pulse rotates the neutron spins by $\frac{\pi}{2}$ bringing them into the plane perpendicular to the static magnetic field . The spins then undergo free precession in the intermediate region at the Larmor frequency, accumulating a phase over time.

In the second RF region, a second pulse is applied. The final spin state depends on the phase difference accumulated between the neutron precession and the RF field. When the RF frequency matches the Larmor frequency, the pulses combine constructively, maximizing the signal. A mismatch in frequency results in a phase shift, leading to a reduction in the detected signal and giving rise to the characteristic Ramsey interference pattern[3].

Based on the measured phase of the Ramsey fringe, it can be determined whether an additional axion-induced phase shift is present. These fringes arise when the outgoing polarization, P is plotted against the detuning, $\Delta = \omega_1 - \omega_L$, where ω_1 is the applied frequency. The outgoing polarization is the measured variable in this experiment. Assuming an idealised scenario, with input polarization $P_i = +1$ and instantaneous $\frac{\pi}{2}$ flips due to the RF pulses, we would obtain output polarization as a function of detuning:

$$P(\Delta) = -\cos(\Delta T), \tag{4}$$

where T is the precession time, which can be expressed as $T = L/v$ where L and v are the precession length and neutron speed respectively.

To account for imperfections in a realistic scenario, the formula must be changed to

$$P(\Delta) = C\cos(\Delta T + \phi_0) + C_0, \tag{5}$$

where C is the fringe contrast, ϕ_0 is a phase shift and C_0 is a term accounting for small offsets in the polarization.

The additional field caused by the ALPs would contribute to the phase shift by $\delta\phi = \gamma T \delta B$, where δB is the additional effective pseudomagnetic field caused by the axion. This would correspond to a horizontal shift of the Ramsey fringes.

As these shifts are very small, it is necessary to ensure maximal sensitivity and precision.

This can be achieved in part by carrying out analysis not on the entire Ramsey fringe but near the points of steepest slope. These are defined as $\Delta T + \phi_0 \approx \frac{\pi}{2}$, due to the behaviour of the cosine function.

By performing a Taylor expansion around such a point Δ_0, we may write that:

$$P(\Delta) \approx a + b(\Delta - \Delta_0), \tag{6}$$

where the slope is $b = \frac{dP}{d\Delta}|_{\Delta_0} = -CT\sin(\Delta_0 T + \phi_0) = \mp CT$.

To determine the slope b, several measurements of the polarization around Δ_0 are taken and a weighted linear fit is performed. The uncertainty of the detuning shift from a single neutron pulse is given by:

$$\sigma_\Delta = \frac{\sigma_a}{|b|}, \tag{7}$$

where σ_a is the uncertainty at the working point, which scales as $\sigma_a \propto \frac{1}{\sqrt{N}}$ where N is the intensity of detected neutrons. Therefore, we obtain that the uncertainty scales such that:

$$\sigma_\Delta \propto \frac{1}{CT\sqrt{N}}. \tag{8}$$

Consequently, the uncertainty of the inferred effective magnetic field shift due to axion interaction scales as

$$\sigma_{\delta B} = \frac{\sigma_\Delta}{\gamma} \propto \frac{1}{\gamma CT\sqrt{N}} \tag{9}$$

In order to minimise this uncertainty and improve the sensitivity of the experiment, the quantity $T\sqrt{N}$ must be maximised[19]. For the purpose of this thesis, C will be assumed to be constant as it depends on magnetics, which is beyond the scope of this thesis.

2.5 Neutron Optics

As mentioned in the previous section, the quantity $T\sqrt{N}$ is sought to be maximised. This can be in part achieved by optimising the neutron optics guide system of HIBEAM, which is the subject of this thesis. Neutrons can be scattered, reflected and diffracted in a manner analogous to electromagnetic radiation. As long as the incident angle of the neutron is less than the critical angle of the material, the neutron will be totally reflected and continue along the desired path. Neutron optics encompass a variety of factors in the materials and geometry of the set-up to maximise the intensity of neutrons at a given point. Given that neutrons are weakly-interacting particles, several principles need to be employed in order to focus a neutron beam. Only the methods used in this thesis will be discussed here.

Firstly, the optics system is coated in neutron-reflective material, known as a supermirror [20] which can take on different levels of reflectivity. This variable is referred to as the m-value of the material, with $m = 0$ being completely absorbing. The m-value is the ratio of the critical wavevector transfer of the supermirror to that of a nickel-coated guide. This is illustrated in Figure 4a.

Neutron supermirrors are composed of alternating layers of materials such as nickel and titanium, where the layer thickness gradually decreases with depth from the reflecting surface. A neutron supermirror diagram is shown in Figure 4b. The main principle underlying supermirrors is the Bragg condition. The gradual variation in layer thickness allows the supermirror to satisfy the Bragg condition for a broad range of neutron wavelengths and incident angles. Longer-wavelength neutrons are reflected near the surface, whereas shorter-wavelength neutrons penetrate deeper into the multilayer structure before undergoing reflection. This is due to the fact that the neutron critical angle depends on its wavelength. [21]

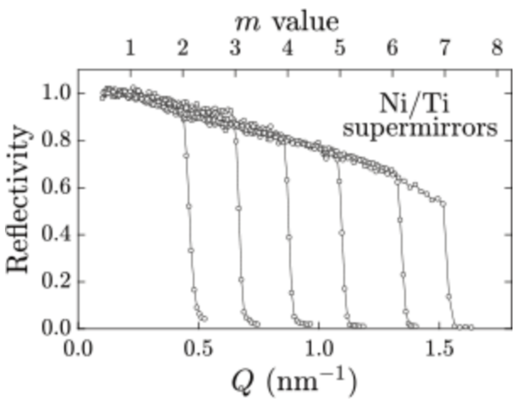

(a) Example m-value data. Credit: SwissNeutronics AG.

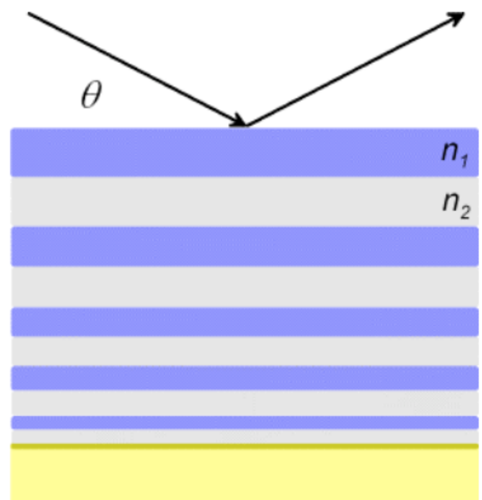

(b) Neutron Supermirror Diagram. Credit: T. Chupp. [22]

Figure 4: Diagrams of sample m-value data and diagram illustrating supermirror working principle.

Secondly, a passive focusing method that can be employed is collimation. This method involves shaping the neutron beam such that the transmitted beam corresponds to the region of highest neutron intensity. Collimators are used to limit the angular divergence and spatial extent of the neutron beam. In this specific setup, the beam size is additionally constrained by the polarizer cell, which has a diameter of 10 cm (see Figure 3). The 10 cm diameter was chosen as a compromise between maximizing neutron acceptance and the practical limitations associated with larger polarizer cells, including cost and magnetic field requirements. Collimators are typically made of absorbing materials, such as gadolinium- or boron-based compounds, often deposited on substrates like polyethylene terephthalate (PETP), or from bulk materials such as borated plastics or metals. Multiple collimators can be arranged in sequence to achieve the desired beam divergence and profile [23].

Thirdly, the shape of the guide also affects the divergence and intensity of the neutron beam. The main shapes are straight, curved, elliptical and tapered. The flat, tapered guide is the simplest way to focus the beam, however, although the flux density increases, the divergence increases also, meaning that as the beam exits the guide, the beam expands quickly. These various guide shapes are shown in Figure 5. The HIBEAM beamline uses an asymmetric elliptical guide which performed better than a symmetric elliptical guide of the same dimensions [10].

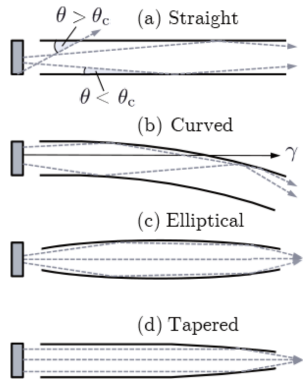

Figure 5: Diagrams of various neutron guide shapes. [23]

3 Methodology

Since the statistical sensitivity scales as $T\sqrt{N}$ the quantity NT^2 proportional to the square of the figure of merit, was used for the optimization. The neutron optics section located between 5.5 m and 15 m relative to the neutron source was optimized. The main focus of this thesis was to collimate the beam into the desired 10 cm diameter while also maximizing the value of the figure of merit. The optimization was entirely conducted using simulations with McStas software. The optimization was carried out in several phases, each phase corresponding to one variable being optimized, independent of the others. Once a variable was optimised, it was set as this optimal value for the subsequent optimization phases.

3.1 Simulation Program

McStas is a neutron ray-tracing simulation package that employs Monte Carlo methods to model neutron transport through instrument components. Monte Carlo methods are used because solving analytically for the complex integral over all parameters is often difficult or unsolvable. Monte Carlo methods provide a numerical approximation of this desired integral.

The main principle underpinning Monte Carlo methods is the law of large numbers. Consider a function $f(u)$ which is finite, continuous and integrable and whose integral is to be computed. The discrete statistical mean value of f in a uniformly sampled interval $a < u < b$ converges to the mathematical mean value of f in that interval. This is expressed explicitly below.

$$\lim_{n\to\infty} \frac{1}{n} \sum_{i=1, a<u_i<b}^{n} f(u_i) = \frac{1}{b-a} \int_a^b f(u)du \tag{10}$$

If the sampling of u_i is random and uniform, this is the Monte Carlo integral method. In the specific case of this thesis work, f corresponds to the dependent variables intensity and time, while u corresponds to the variables changed, for instance the m-value.

In order to optimize the simulation, McStas assigns a weight to each neutron depending on how likely its path is in order to preserve computation power. Each neutron has an initial weight p_0 which is affected by a factor π_j for each component in the instrument j. The condition $0 < \pi_j < 1$ is necessary to ensure that the flux can only decrease as it passes through the instrument. The final neutron weight is shown below.

$$p = p_0 \prod_{j=1}^{n} \pi_j \tag{11}$$

McStas also keeps track of statistical errors. Let $I = \sum_i p_i = N\bar{p}$ be the neutron flux or intensity, where N is the number of neutrons. For the sake of this derivation, the statistical uncertainty assumes a simplification that $p_i \approx \bar{p}$, that $N \geq 10$ and that N follows a normal distribution.

Therefore:

$$\sigma(N) = \sqrt{N}, \tag{12}$$

which leads to:

$$\sigma(I) = \sqrt{N}\bar{p} = \frac{I}{\sqrt{N}}. \tag{13}$$

Assuming that N and p are independent variables, the variance is:

$$\sigma^2(I) = \sigma^2(N)\bar{p}^2 + N^2\sigma^2(\bar{p}) \approx \sum_i p_i^2. \tag{14}$$

McStas keeps track of the following during simulations: $N = \sum_i p_i^0$, $I = \sum_i p_i^1$ and $M_2 = \sum_i p_i^2$.

Another method used by McStas to optimise computational resources is to preferentially simulate neutron trajectories that are more likely to be detected. In this way the computational effort is focused on the most relevant parts of the phase space. This method is known as direction focusing. This assumes that there is a solid angle sector $\Delta\Omega$ of the total 4π solid angle which contains all interesting directions.

Additionally, McStas employs stratified sampling. This ensures equal distribution of events across the entire space being integrated over. The space is partitioned into D sub-spaces, and each will have $r = \frac{N}{D}$ events [24].

3.2 Simulation Variables

This optimization process was based on a pre-existing non-optimized version of the McStas model of the short-HIBEAM, which is displayed below in Figure 6 [25] . The focus of this thesis is the neutron optics guide section, which already consisted of an asymmetric elliptical guide.

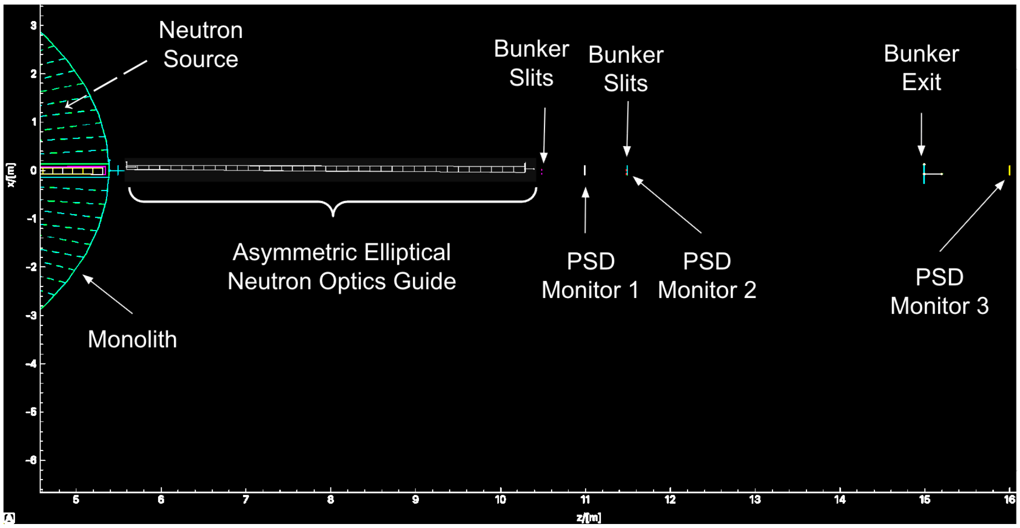

Figure 6: McStas rendering of original HIBEAM design before this thesis work's optimization. The neutron source (ESS Butterfly) is not pictured in this rendering and is located further to the left.

The neutron source used is the ESS Butterfly component running at 2 MW. The neutron optics system consists of an asymmetric elliptical guide together with several collimators. Several monitors are used to check the beam's intensity and divergence at different points along the beam. These monitors are only for simulation purposes and do not correspond to any actual components in the beamline. In the final experimental setup, the only physical detector will be positioned at the end of the beamline

In the first phase of the optimization, the reflectivity of the neutron guide surface was optimised. This is referred to as the m-value and in the McStas software takes on values equal to or greater than 0, where 0 is completely absorbing. Integer m-values between 1 and 4 were tested.

Next, the beam was collimated to obtain the desired beam dimensions of 10 cm. The beam intensity was concentrated in the corners, as can be seen in Figure 7. The first phase of collimation was to split the beam into four corners of equal area. Each corner is respectively referred to as Upper-Left, Upper-Right, Lower-Left and Lower-Right. Figure 7 shows a beam profile from a Position Sensitive Detector (PSD) monitor the different corner windows to be tested. Each window was tested for the value of NT^2 and a qualitative analysis of the beam at various distances from source was also conducted. Since the selected beam region needed to be transmitted efficiently through the downstream Ramsey setup, the dimensions and positions of subsequent components, in particular the Alpha–Omega setup described in Section 3.3, were adjusted accordingly. An additional PSD monitor was placed immediately after the collimator to verify the beam profile after collimation. The collimation was rectangular at this phase and was adjusted to be circular in the following phase.

In addition, the location of the collimator was tested for different locations along the beamline at 15 m and at 16 m relative to the source, with circular collimation of diameter 10 cm. The magnetically shielded section of the beamline is expected to extend either from 15 m to 25 m or from 16 m to 26 m relative to the neutron source. The locations of the components following the collimator were also adjusted to capture as much of the beam as possible.

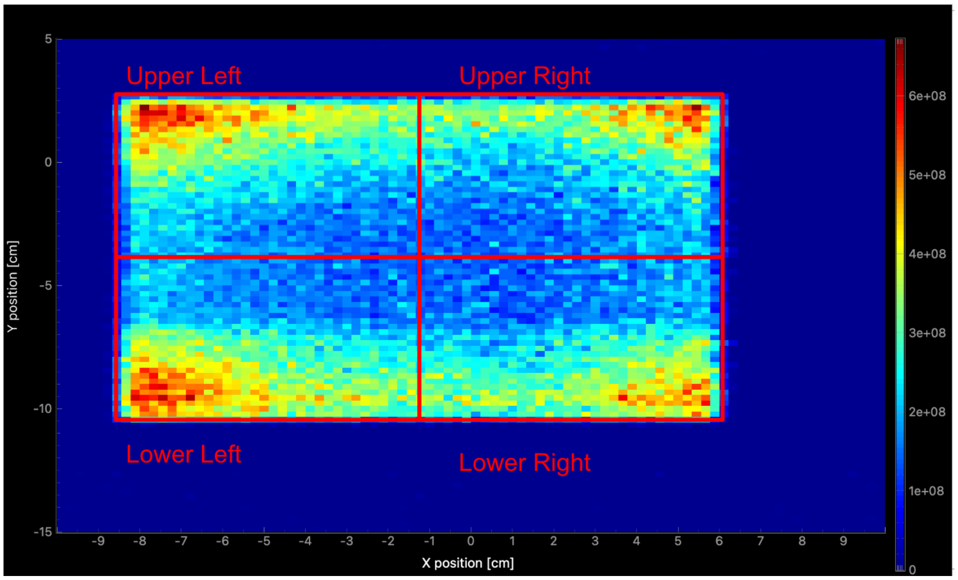

Figure 7: Example of the pre-collimation beam profile for $m = 4$ at the first detector (PSD Monitor 1) , showing the approximate corner regions used for the Phase 2 collimation optimization.

3.3 Method for determining NT^2

In order to evaluate the figure of merit, the time of flight T of the individual neutrons needed to be determined. This was accomplished by placing two virtual detectors, named Alpha and Omega at the desired locations, corresponding to the locations of the RF spin flippers. They were chosen to be 10 cm in diameter due to the restriction on beam size of the polarizer cell. These detectors are not physical components of the final experimental setup and were used solely for neutron optics optimization purposes. These detectors, along with the pre-optimised beamline design is shown below in Figure 8. Note that the Alpha and Omega components are exaggerated in this diagram for easier viewing.

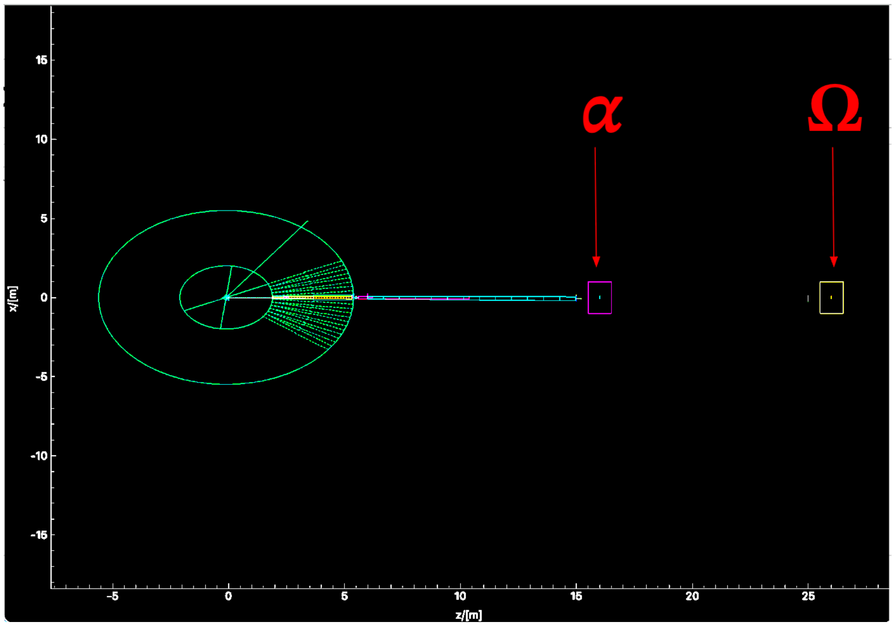

Figure 8: Short-HIBEAM beamline with Alpha-Omega set-up viewed from *x*-*z* plane.

Each neutron in the simulation is tagged with a tracking identifier. As each neutron passes detector Alpha a variable is set to TRUE to tag that neutron as having passed through detector Alpha. This ensures that every neutron whose data is recorded at detector Omega has also passed through detector Alpha. In addition, when a neutron passes through detector Alpha, the time is reset to zero, such that the recorded time at detector Omega will not need to be adjusted.

The run produces two data files, one from each detector Alpha and Omega containing the time of flight and statistical weight of each neutron.

3.3.1 Method for determining optimal placement of Alpha and Omega

Due to the beam diverging non-uniformly the further away from the source, adjustments must be made to capture as much of the intensity as possible.

This was accomplished with a Python script taking the data file for the Alpha and Omega PSD monitors from a simulation run. Each point in the files was taken as a possible centre of a 10 cm circle and the intensity captured within that circle was calculated. The coordinates of the centre of the circle with the greatest captured intensity were taken to set the centre of the Alpha and Omega components. This process was completed once for Alpha and once for Omega. The x and y for these components were adjusted accordingly before running the simulations.

3.4 Workflow

For each simulation variable tested, the following procedure follow. Firstly, the necessary changes to the variable are made in the main McStas instrument file. Then, ten runs, each with a unique random seed were performed with 10^7 neutrons simulated. Ten runs were chosen to provide a sufficiently large dataset for averaging while remaining compatible with the available computational time constraints. These runs produce data files for each detector in the McStas instrument, which are read by a Python script that calculates the corresponding NT^2 value for the selected set of parameters. Then, the mean average and standard deviation of these ten runs was calculated. Once this process was completed for each desired value of a specific variable, their average values and standard deviations were plotted against each other to determine the optimal value of the variable.

Several detectors were placed along the beamline at particular locations of interest for the whole optimization. Firstly, a PSD detector is placed at the monolith exit (around 5.5m relative to source), with dimensions 10 cm by 10 cm. It shows the beam essentially directly from the source. The Alpha-Omega set-up includes a PSD monitor for each Alpha and Omega placed respectively at 16 m and 26 m. Both have a 10 cm diameter.

For Phase 2 of the optimization (corner-selective collimation), another PSD director was placed right after the collimation for ease of viewing the collimation before the beam diverges further down the beamline. This placement was at 5.51 m for Phase 2, then adjusted for Phase 3 when testing various positions for the collimator, as described in Section 3.3.1.

4 Results

With the optimization process being performed in several incremental phases, improvements were obtained in each phase. The results are presented in chronological order of how the optimization was carried out.

4.1 Phase 1: *m*-value optimization

The *m*-values displayed below in Figure 1 are the result of running the simulation ten times with a different random seed each time. The results were averaged and the error bars indicate the standard deviation over the runs for each point.

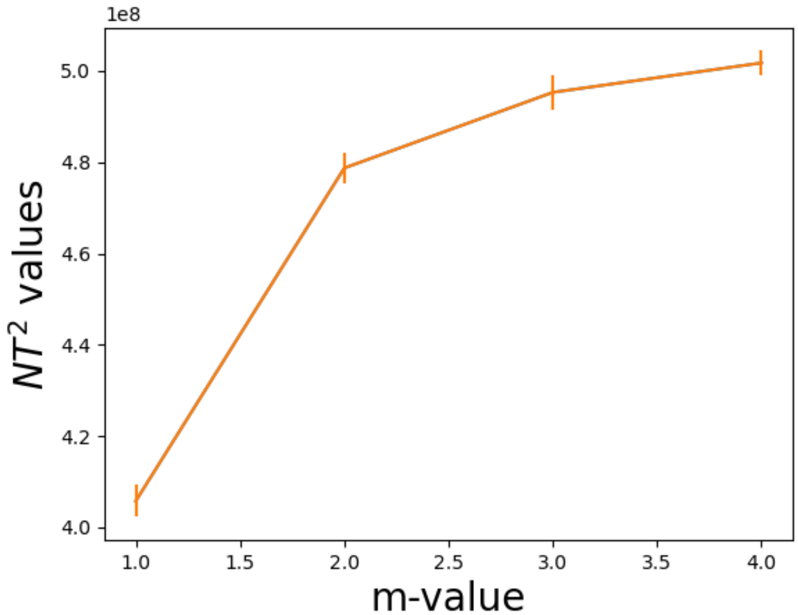

Figure 9: Results of NT^2 values for varying m-value of neutron guide.

A sample of the detector data for $m = 4$ is shown below in Figure 10, at the monolith exit (5.5 m), at Alpha (16 m) and Omega (26 m).

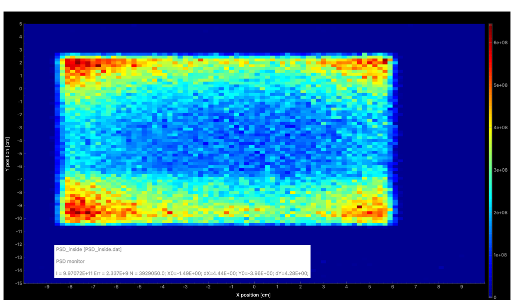

(a) Beam with $m = 4$ at source exit at 5.5 m.

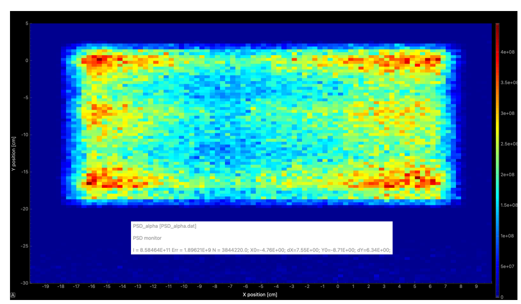

(b) Beam with $m = 4$ at detector Alpha at 16 m.

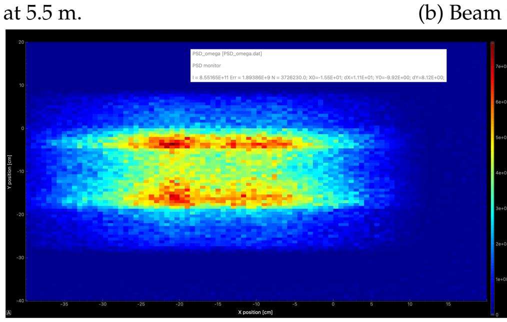

(c) Beam with $m = 4$ at detector Omega at 26 m.

Figure 10: Sample results of neutron intensity of the beam with $m = 4$ neutron guide, at source exit, Alpha detector and Omega detector (5.5 m , 16 m and 26 m relative to the source respectively).

4.2 Phase 2: Corner-Selective Collimation

The results of corner-selective rectangular collimation at 5.5 m from the source with $m = 4$ neutron guide are displayed below in Figure 11.

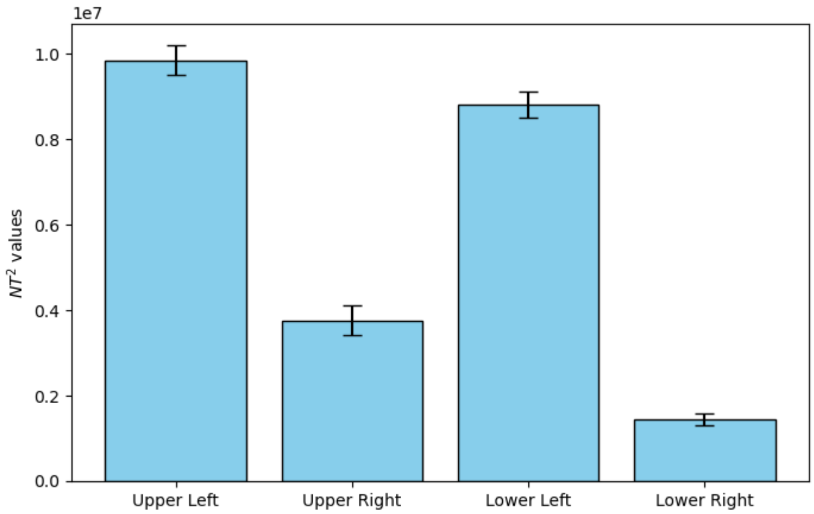

Figure 11: Results of NT^2 values for corner collimation.

A sample of the detector data for the Upper Left corner collimation set-up is displayed below in Figure 14. It can be interpreted as a cross-section in the x-y plane of what the beam looks like at different locations along the beamline, with Subfigure 16b being the closest to the source and Subfigure 12d being the furthest from the source.

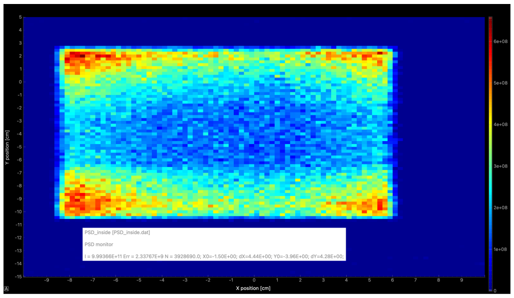

(a) Beam before collimation.

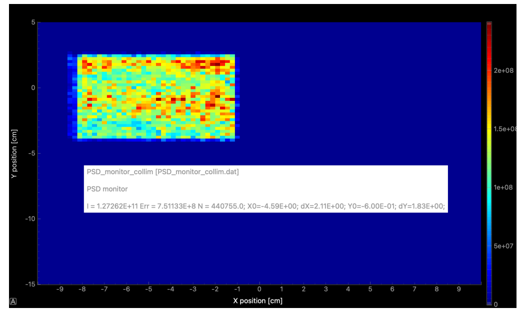

(b) Beam immediately after collimation.

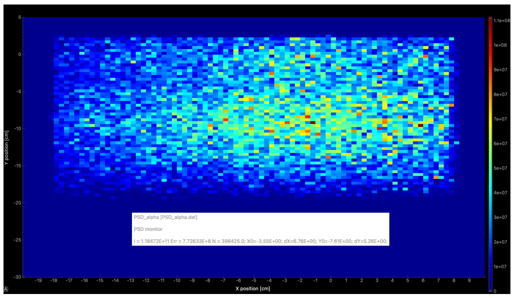

(c) Beam at Alpha Detector.

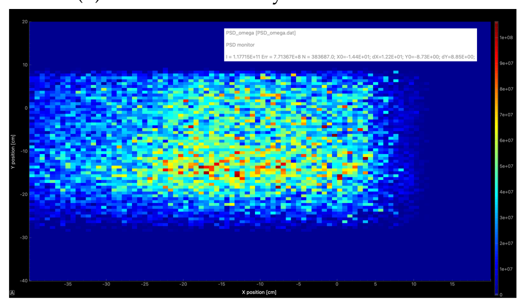

(d) Beam at Omega Detector.

Figure 12: Sample results of neutron intensity of the beam before collimation, immediately after Upper Left collimation, at Alpha and Omega detectors (5.5 m, 5.51 m, 16 m and 26 m relative to the source respectively).

4.3 Phase 3: Collimator Location

The rectangular collimator was replaced by a circular collimator with diameter 10 cm at the optimal circle location using the method described in Section 3.3.1. A sample of the result of this process is shown below in Figure 13.

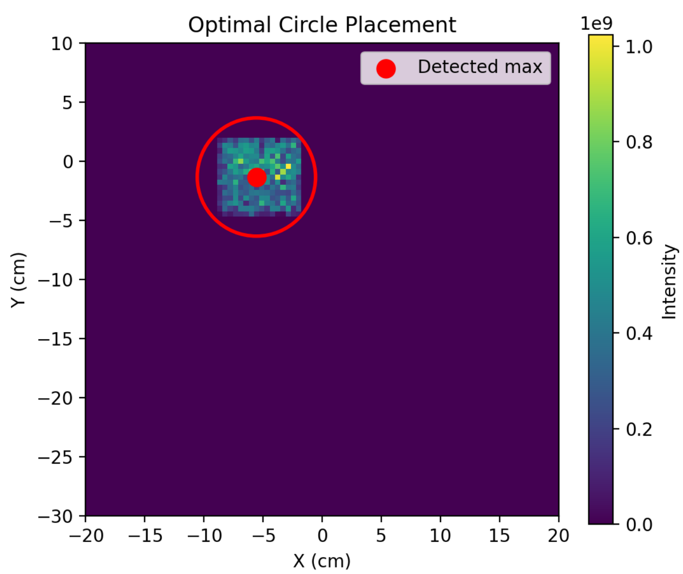

Figure 13: Placement of circular collimator relative to Upper Left rectangular collimation.

The same procedure for the optimal location of the Alpha and Omega detectors was performed, of which a sample is displayed below:

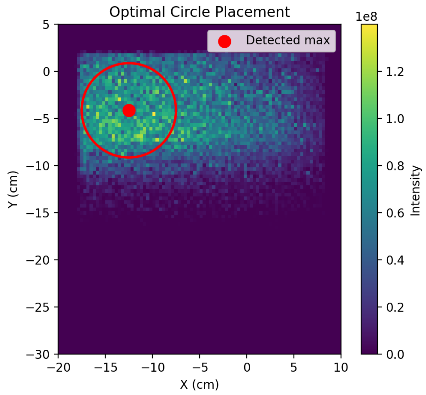

(a) Optimal Location of Alpha.

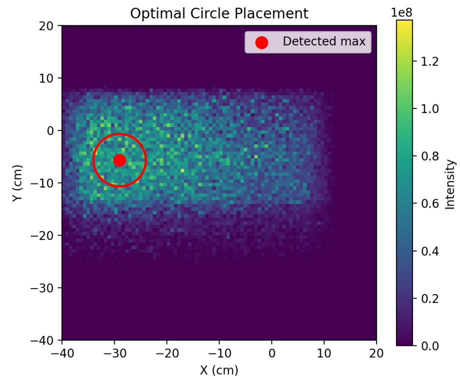

(b) Optimal Location of Omega.

Figure 14: Optimal location of circular Alpha and Omega components to maximise beam captured.

The results of location-selective collimation at 15 m and 16 m are shown below in Figure 15.

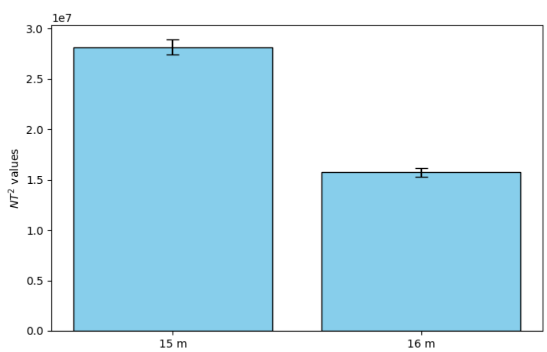

Figure 15: Results of NT^2 at 15 m and 16 m from the source.

A sample of detector data for the optimal collimator location of 15 m is displayed below in Figure 16. An additional PSD monitor was added 0.1 m after the collimation to visualise more easily, as well as the beam at Alpha and Omega.

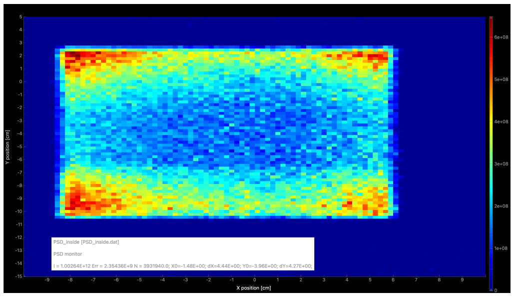

(a) Beam before collimation

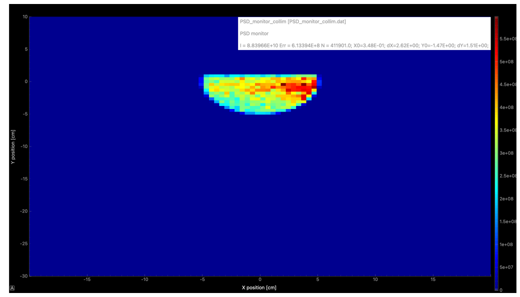

(b) Beam immediately after collimation

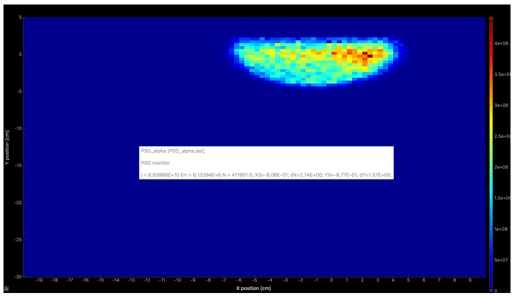

(c) Beam at Alpha detector

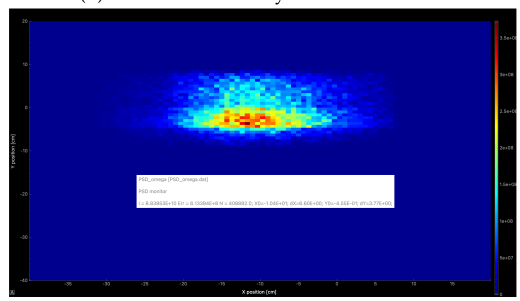

(d) Beam at Omega Detector

Figure 16: Sample results of neutron intensity of the beam before collimation, immediately after Upper Left collimation, at Alpha and Omega detectors (15 m, 15.1 m, 16 m and 26 m relative to the source respectively).

5 Discussion and Conclusions

5.1 Phase 1: *m*-value optimization

There is a clear peak on Figure 9 at $m = 4$, as expected by theory, with a FOM of $5.1 \cdot 10^8 \pm 2.6 \cdot 10^6$. However, it can be seen that although increased the reflectivity from $m = 1$ to $m = 2$ offers some improvement in the FOM, subsequent increases in m offer diminishing returns. This thesis recommends the choice of $m = 3$ or $m = 4$ depending on cost considerations.

5.2 Phase 2: Corner-Selective Collimation

On Figure 11, it can be clearly seen that the Upper Left and Lower Left corners provided the highest values for NT^2, with Upper Left being slightly larger. From this, it is decided that the Upper Left corner will be selected and further optimized due to its FOM value being the largest, $9.9 \cdot 10^6 \pm 3.4 \cdot 10^5$.

5.3 Phase 3: Collimator Location

From Figure 15, it can be seen that the value for the placement of the collimator at 15 m relative to the source is larger, with a FOM of $2.8 \cdot 10^7 \pm 7.2 \cdot 10^5$.

5.4 Final Specifications Summary

The table below summarises the findings of this thesis. Figure 17 shows a McStas rendering after implementing all the changes to the beamline. Various detectors used during the optimization process have been omitted for clarity.

Table 1: Summary of the optimization results obtained during the different stages of the study. The first row corresponds to the optimization without collimation, while the second and third rows correspond to configurations with collimation. The collimation dimensions are $-0.087\,\text{m} \leq x \leq -0.011\,\text{m}$ and $-0.034\,\text{m} \leq y \leq 0.027\,\text{m}$.

Variable	**Optimal Value**	NT^2 **Value**
m-value	4	$5.1 \cdot 10^8 \pm 2.6 \cdot 10^6$
Collimation Dimensions	$-0.087\text{m} \leq x \leq -0.011\text{m}$ $-0.034\text{m} \leq y \leq 0.027\text{m}$	$9.9 \cdot 10^6 \pm 3.4 \cdot 10^5$
Collimator Location	15 m	$2.8 \cdot 10^7 \pm 7.2 \cdot 10^5$

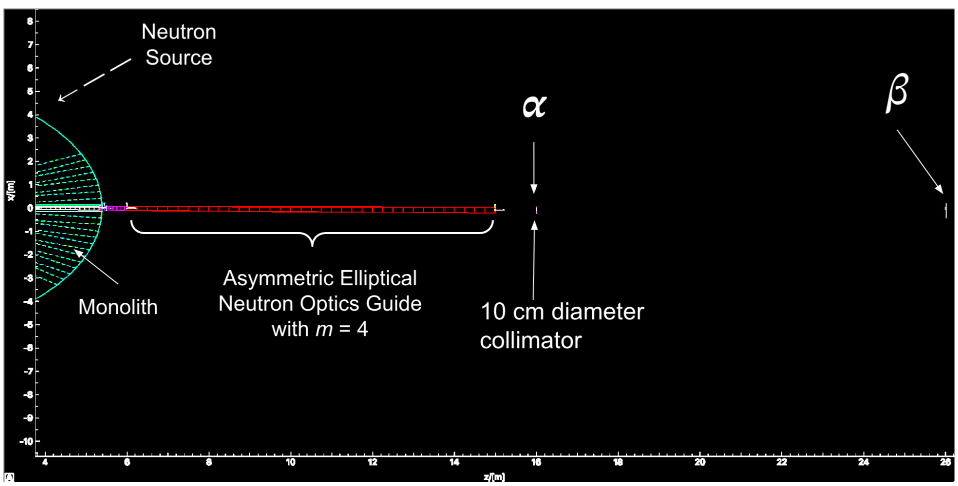

Figure 17: McStas rendering of final HIBEAM design after this thesis work's optimization. The neutron source (ESS Butterfly) is not pictured in this rendering and is located further to the left.

6 Outlook

This thesis successfully developed and optimized the neutron optics design for the short-HIBEAM beamline. The NT^2 value obtained without collimation provides an estimate of the sensitivity of the short-HIBEAM setup for neutron–antineutron oscillation searches, while the NT^2 values obtained with collimation are relevant for the sensitivity of the ALP search. These calculations are important for the development and proposal of the short-HIBEAM beamline.

Ten trials were performed and averaged for each variable tested. More trials would increase reliability in the results, as well as decrease uncertainties.

Further limitations of this simulation work include that gravity was ignored for all components, and that each component in the simulation was instructed to restore any neutrons that it may absorb. This creates a simulation that is more idealised than the real world outcomes. By introducing more real-world limitations such as the ones mentioned above, this simulation would be of better quality and reliability, but this was beyond the scope of this thesis work.

References

[1] R.L. Workman and et al. “Review of Particle Physics”. In: *Progress of Theoretical and Experimental Physics* 2022 (2022), p. 083C01. DOI: 10.1093/ptep/ptac097.

[2] R. D. Peccei and H. R. Quinn. “CP conservation in the presence of instantons”. In: *Physical Review Letters* 38 (1977), pp. 1440–1443. DOI: https://doi.org/10.1103/PhysRevLett.38.1440.

[3] N. F. Ramsey. “A Molecular Beam Resonance Method with Separated Oscillating Fields”. In: *Physical Review* 78.6 (1950), pp. 695–699. DOI: 10.1103/PhysRev.78.695.

[4] P. K. Willendrup and et al. *McStas - A neutron ray-trace simulation package*. 2026. URL: https://www.mcstas.org/.

[5] European Spallation Source. *How the Accelerator Works*. 2026. URL: https://ess.eu/accelerator/how-it-works.

[6] H. Tatsumoto and et al. “Design status of the ESS cryogenic moderator system”. In: Lund, Sweden: IOP Conference Series: Materials Science and Engineering, 2020. DOI: 10.1088/1757-899X/755/1/012101.

[7] H. Abele and et al. “Particle physics at the European Spallation Source”. In: *Physics Reports* 1023 (2023), pp. 1–84. DOI: 10.1016/j.physrep.2023.05.003. URL: https://www.sciencedirect.com/science/article/pii/S037015732300134X.

[8] R. Garoby and et al. “The European Spallation Source Design”. In: *Physica Scripta* 93.1 (2018), p. 014001. DOI: 10.1088/1402-4896/aa9bff.

[9] K. H. Andersen and et al. “The instrument suite of the European Spallation Source”. In: *Nuclear Instruments and Methods in Physics Research Section A: Accelerators, Spectrometers, Detectors and Associated Equipment* 957 (2020), p. 163402. DOI: 10.1016/j.nima.2019.163402. URL: https://www.sciencedirect.com/science/article/pii/S0168900220300097.

[10] V. Santoro and et al. “The HIBEAM instrument at the European spallation source”. In: *Journal of Physics G: Nuclear and Particle Physics* 52.040501 (2025). DOI: 10.1088/1361-6471/52/4/040501. URL: https://iopscience.iop.org/article/10.1088/1361-6471/adc8c2.

[11] M. Baldo-Ceolin and et al. “A new experimental limit on neutron-antineutron oscillations”. In: *Experimental Physics* 63 (1994).

[12] J. Lu and et al. “Advanced Manufacturing and Instrumentation for Neutron Chopper Design”. In: *Journal of Young Investigators* (2020).

[13] P. Fierlinger et al. “Proposal for a Ramsey Neutron-Beam Experiment to Search for Ultralight Axion Dark Matter at the European Spallation Source”. In: *Physical Review Letters* 133 (18 2024), p. 181001. DOI: 10.1103/PhysRevLett.133.181001. URL: https://link.aps.org/doi/10.1103/PhysRevLett.133.181001.

[14] C. B. Adams and et al. “Axion Dark Matter”. In: (2022). DOI: 10.48550/arXiv.2203.14923. arXiv: 2203.14923 [hep-ex]. URL: https://arxiv.org/abs/2203.14923.

[15] LHCb Collaboration. “Observation of charge–parity symmetry breaking in baryon decays”. In: *Nature* 643 (2025), pp. 1223–1228. DOI: 10.1038/s41586-025-09119-3. URL: https://www.nature.com/articles/s41586-025-09119-3.

[16] L. Bergström. “Dark matter candidates”. In: *New Journal of Physics* 11.10 (2009). DOI: 10.1088/1367-2630/11/10/105006. URL: https://iopscience.iop.org/article/10.1088/1367-2630/11/10/105006.

[17] I.G. Irastorza and J. Redondo. “New experimental approaches in the search for axion-like particles”. In: *Progress in Particle and Nuclear Physics* 102 (2018). DOI: https://doi.org/10.1016/j.ppnp.2018.05.003. URL: https://www.sciencedirect.com/science/article/abs/pii/S014664101830036X.

[18] J. A. Dror et al. “On the Sensitivity of Spin-Precession Axion Experiments”. In: *Physical Review Letters* 130.18 (2022), p. 181801. DOI: 10.1103/PhysRevLett.130.181801. URL: https://www.researchgate.net/publication/364526142_On_the_Sensitivity_of_Spin-Precession_Axion_Experiments.

[19] L. Persson et al. “A Simulation Framework for Ramsey Interferometry”. In: (2026). arXiv: 2603.24049 [physics.ins-det]. URL: https://arxiv.org/abs/2603.24049.

[20] F. Mezei. “Novel polarized neutron devices: supermirror and spin component amplifier”. In: *Communications on Physics* 1.3 (1976), pp. 81–85.

[21] A. Boothroyd. *Principles of Neutron Scattering from Condensed Matter*. Oxford Academic, 2020. URL: https://doi-org.ludwig.lub.lu.se/10.1093/oso/9780198862314.003.0009.

[22] T. Chupp. *Neutron Optics and Polarization*. https://www.ncnr.nist.gov/summerschool/ss09/pdf/Chupp_FP09.pdf.. University of Michigan.

[23] A. Erko et al., eds. *Modern Developments in X-Ray and Neutron Optics*. NATO Science for Peace and Security Series B: Physics and Biophysics. Berlin: Springer, 2008. ISBN: 9783540745600. DOI: 10.1007/978-3-540-74561-7.

[24] P. Willendrup et al. *User and Programmers Guide to the Neutron Ray-Tracing Package McStas, version 3.6*. Version 3.6.5. Technical University of Denmark. 2800 Kongens Lyngby, Denmark, Jan. 2026. URL: https://www.mcstas.org/documentation/manual/mcstas-3.6.5-manual.pdf.

[25] M. Holl and L. Persson. *ALP.instr*. https://github.com/HIBEAM-NNBAR/McStas_HIBEAM/blob/main/ALP/alp.instr. 2026.